ADVANCED MATERIALS INTERFACES
Open Access
www.advmatinterfaces.de

Transport of Hydrogen Through Anion Exchange Membranes in Water Electrolysis

*Andre Klinger, Oscar Strobl, Hannes Michaels, Michael Kress, Nemanja Martic, Anna Maltenberger, Benjamin Britton, Andrew Belletti, Rüdiger-A. Eichel, and Guenter Schmid**

The transport of hydrogen through an anion-exchange membrane (AEM) is analyzed by *in-line* product gas analysis in a large dynamic range (0.1–2 Acm^{-2}) at ambient pressure and correlated to *ex situ* membrane properties, including volumetric electrolyte uptake, dimensional swelling and diffusivities. A commercial AF3-HWK9-75-X membrane from Ionomr Innovations Inc. is characterized and employed in a 25 cm^2 electrolyzer cell, which is operated for 56 h at 60 °C in 1 M KOH solution. A model of the membrane is developed, based on a combination of existing theoretical knowledge regarding liquid electrolytes and measured properties of the membrane. The model is employed to quantify the transport parameters through the membrane and the porous electrode. The hydrogen transport through the membrane is 770 times slower than through the electrode. The anion-exchange membrane permits a low degree of gas crossover, with a hydrogen-in-oxygen concentration of 0.37 % at 2 Acm^{-2}. The model indicates that modifying the membrane's microstructure has a more pronounced effect on the gas crossover than altering the swollen thickness. A correlation is derived to estimate the polymer diffusivity from the derived effective diffusivity through the membrane, which allows the determination of preferred membrane properties to lower hydrogen crossover.

1. Introduction

Hydrogen has been used over the past century primarily as a chemical feedstock in refinery processes, ammonia and methanol production or the direct reduction of iron ore. In 2022 the refining and industry sector (chemicals and steel) alone accounted for ≈95 Mt hydrogen per year with an average increase of ≈ 3 % since 2018.[1–3] Future potential use cases, such as power generation, transport or synthetic fuels, have not been established yet and further increase especially the demand for green hydrogen. In order to serve this future demand, the amount of hydrogen being produced by electrolysis needs to increase, but decrease in cost as well, in order to prove economical feasibility. In 2021 the levelized cost of hydrogen (LCOH) for fossil-based hydrogen was in the range of 1.0–3.0 USD/kg_{H_2}, whereas in the case of electrolysis and low-emission electricity the price was 3.4–12 USD/kg_{H_2}.[3] These cost arise from state-of-the-art electrolysis technologies such as proton exchange membrane water electrolysis (PEMWE) or alkaline water electrolysis (ALKWE). 40–50 % total electrolyzer plant investment cost arise from the electrolyzer stack only, according to the Irena 2020 report.[4] In addition, the scarcity of abundant raw metals such as iridium limits the production of PEM electrolyzers and increase cost due to increasing demand. Potential future technologies such as anion exchange membrane water electrolysis (AEMWE) using advanced and significantly cheaper materials enable significantly lower stack cost and higher production capacities. AEMWE combines the benefit of not using scarce noble metals such as iridium as an oxygen evolution catalyst, while maintaining high hydrogen production rates per stack at high efficiencies. The enabling component of such an AEMWE-stack is the anion exchange membrane. In contrast to a PEMWE, the membrane is operated in mild alkaline conditions. Compared to an alkaline electrolyzer separator, the membrane is ion-conducting only 25–100 μm thick and has no macropores. The electrode reaction occur according to Equations (1) and (3)

A. Klinger, O. Strobl, H. Michaels, M. Kress, N. Martic, A. Maltenberger, G. Schmid
Siemens Energy Global GmbH and Co. KG
Schuckertstrasse 2, 91058 Erlangen, Germany
E-mail: guenter.schmid@siemens-energy.com
B. Britton, A. Belletti
Ionomr Innovations Inc.
2386 E Mall Unit 111, Vancouver BC V6T 1Z3, Canada
R.-A. Eichel
Forschungszentrum Jülich GmbH Institut für Energie- und Klimaforschung Grundlagen der Elektrochemie (IEK-9)
Wilhelm-Johnen-Straße, 52428 Jülich, Germany

The ORCID identification number(s) for the author(s) of this article can be found under https://doi.org/10.1002/admi.202400515

DOI: 10.1002/admi.202400515

and act as source terms for the evolving product gases at the interface between the membrane, catalyst and liquid electrolyte.

$$Cathode: 2H_2O + 2e^- \rightarrow H_2 + 2OH^- \quad E_c^\circ = -0.83\,V \tag{1}$$

$$Anode: 2OH^- \rightarrow \frac{1}{2}O_2 + H_2O + 2e^- \quad E_a^\circ = -0.40\,V \tag{2}$$

$$H_2O \rightarrow O_2 + H_2 \quad \Delta E_{ac}^\circ = -1.23\,V \tag{3}$$

In recent years, conductivities and chemical stability of anion exchange membranes have been optimized to achieve enhanced operational performance and durability in alkaline conditions, resulting in reduced degradation rates.[5–8] Nevertheless, the phenomenon of gas crossover, which results in mixing of the product gases oxygen and hydrogen is only sparsely reported for AEM water electrolysis applications.[9–11] The mixing of hydrogen and oxygen gas potentially leads to hydrogen levels approaching the lower explosion limit of 4 % hydrogen in oxygen. In order to mitigate safety risks and prevent the formation of an explosive mixture, a threshold of 2 % is typically employed.[12,13] Moreno–González et al. demonstrated a hydrogen-in-oxygen concentration of 0.4 % with an applied steady-state current density of 0.6 Acm^{-2} and a temperature of 70 °C over a period of over 5000 h using a polybenzimidazol membrane (AF2-HWP8-75-X) from Ionomr Inc.[10] Nevertheless, greater attention has to be paid to gas purities at partial load operation, such as during startup/ and shut-down procedures. From studies of gas crossover in PEM- and ALKWE it is known, that the magnitude of different transport processes, such as convection, diffusion, or electroosmotic drag (**Figure 1**), changes with cell design, membrane chemistry or the direction of ionic transport.[8,14–17] For example, the direction of electroosmotic drag, which increases with current density, is reversed in comparison to PEM systems. In general, the magnitude of these transport processes is influenced by membrane properties, including thickness, liquid content and the permeability of hydrogen through the membrane.

While a thick membrane reduces crossover in PEM-electrolysis significantly, high thickness swelling introduces mechanical stress at the contacting points between electrode and membrane, potentially damaging the membrane or blocking channels at the cathode for the hydrogen to escape.[13] In this study a mass transport model for the cross over of hydrogen is derived from a mass balance of hydrogen through the membrane and into the gas phase to quantify an effective hydrogen diffusivity. The model is parametrized using *ex situ* membrane properties of a commercial membrane such as swelling, water uptake and hydration state in respect to the operating conditions (temperature and lye concentration). The influence of operating conditions, transport properties of the electrode and the microstructure of the membrane are discussed Since only a couple of membrane chemistries are available on industrial relevant roll width of > 30 cm, the model structure allows an extension of the study with the above-mentioned chemistries. Applying the model to *in situ* experimental data allows the estimation of kinetic transport properties such as the mass transport coefficient of the electrode and the effective diffusivity of hydrogen through the membrane. The relevance of these properties on the partial load capability also under pressurized conditions is finally discussed and implications for future improvement are drawn.

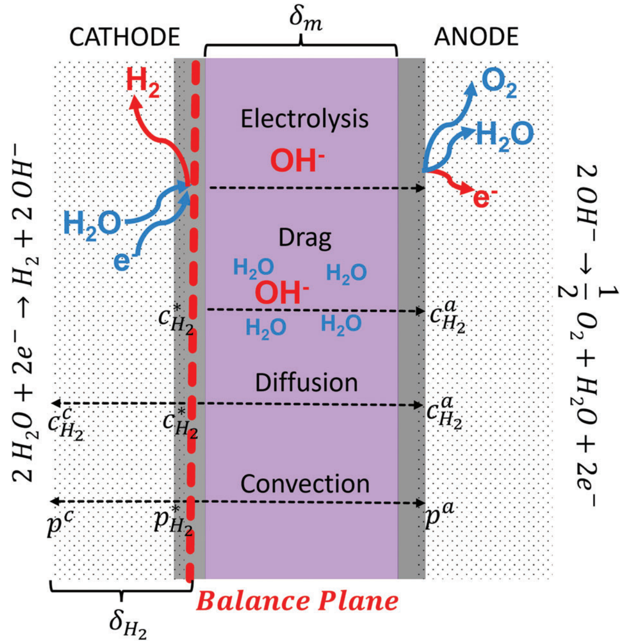

Figure 1. Potenial mass transport processes of hydrogen during electrolysis operation: mass transport of hydrogen into bulk solution, convection, diffusion and electroosmotic drag. δ_{H_2} as concentration boundary layer of hydrogen, δ_m as membrane thickness, c* and p* as concentration and pressure at the catalyst particle, c^c and c^c as equilibrium concentration and pressure.

2. Experimental Section

2.1. Materials

The reinforced membrane (AF3-HWK9-75-X) and ionomer (AP3-HNN9) utilized in this study were procured from Ionomr Innovations Inc. The catalyst employed is a platinum black (Pt). The requisite materials, namely $Ni(OH)_2$, $AgNO_3$, $NaNO_3$, and KBr, were procured from Sigma-Aldrich. A 1M KOH solution was procured from ThermoFisher. The water utilized for all experimental procedures and cleaning steps was Type 1 ultrapure water purified using the Milli-Q Integral water purification system with a resistivity of (18 $M\Omega \cdot cm$). Hydrogen, helium, and argon gases were obtained from AirLiquide.

2.2. Electrode Fabrication

The membrane-electrode assembly consists of a combination of CCS and CCM configuration, with the anode applied directly to the membrane. The cathode electrode was applied onto a Siemens Energy porous transport layer (PTL) with a porosity of 82 % and a thickness of 800 μm, manufactured from 316L steel. The coated PTL was utilized at the cathode, while an uncoated PTL was employed at the anode to facilitate electrical contact. The active area of the electrode was 25 cm^2. The catalyst powder for

Table 1. Initial membrane properties.

Membrane	Thickness μm	ASR / mΩ/;cm^2	Delivery state counter ion	Reinforcement
AF3-HWK9-75-X	75	<190	Cl^- /I^-	Woven PEEK

the anode and cathode electrodes is combined with an ionomer-binder solution prepared in-house and homogenized in a speed mixer (DAC 150, Hausschild) three times for 1 min at 3500 rpm. The resulting ink exhibits a catalyst-to-ionomer ratio of 9:1 in the dry electrode. The anode was applied directly to the membrane via blade coating (Model 288, Erichsen) with a wet film thickness of 50 µm. The coating speed and the placement of the membrane were controlled with the aid of a Coatmaster 510 (Erichsen) and a vacuum chuck. The catalyst loading of the resulting anode layer was $\approx 2.3\ mg\,cm^{-2}$ of $Ni(OH)_2$. The cathode CCS was prepared via transfer printing. The paste is applied directly to a Kapton foil via blade coating. Subsequently, the stainless steel felt is positioned on the wet film and subjected to a defined pressure of 1 bar. The resulting electrode exhibited a catalyst loading of $\approx$ 2.3 $mg\ cm^{-2}$ of Pt. The coated felt was dried in an oven at 180 °C for 30 min. Prior to cell testing, the MEA underwent an ion exchange process for 24 h in 1 M KCl, followed by another 24 h in 1 M KOH, both at ambient temperature as instructed by the membrane manufacturer.

2.3. Setup for Electrochemical Cell Tests

The test rig comprises two distinct electrolyte cycles (Figure S1, Supporting Information), each equipped with a buffer tank that serves as a gas stripper. An electrolyte solution with a concentration of 1 M KOH and a flow rate of 200 $mLmin^{-1}$ was used. The temperature of the feed was set to 60 °C on either side of the electrolysis cell. The cell is operated at ambient pressure. The product oxygen gas, which contains hydrogen impurities, was dried and analyzed by a gas chromatograph (Trace 1310, Thermo Scientific) utilizing heat conductivity sensors and argon as carrier gas. For the electrochemical measurements, the cell was connected to a potentiostat (Autolab PGSTAT302N, Metrohm) for data logging. A power supply (GH10-100, TDK) was employed as the current source. In order to condition the membrane, a polarization curve in accordance with the EU Harmonic for high-performance electrolyzers (up to 2 Acm^{-2}) was employed.[18] In order to measure the hydrogen gas impurities at varying current densities (**Table 1**), different measurement times at each current step were utilized to allow the system to stabilize, particularly at low current densities.

2.4. Membrane Characterization

The membrane employed in this study was an AF3-HWK9-75-X, procured from Ionomr Innovations. The suppliers' membrane properties are presented Table 1.[19] A PEEK woven reinforcement is incorporated into the membrane structure. The membrane is shipped on a roll and on a liner, ensuring secure adhesion during the coating process. For membrane characterization, the membrane was carefully peeled off the liner.

2.4.1. Dimensional Swelling

The in-plane (x,y)-swelling of membranes was evaluated using an optical microscope (VHX 6000, Keyence). The membrane samples were cut into pieces measuring 8×10 mm. The samples were positioned between two glass slides and the precise dry dimensions were recorded using the integrated software of the microscope. Subsequently, the membrane samples were immersed in the designated medium (water, 0.1 or 1 M KOH) for a period of 24 h prior to repeating the measurement. To prevent the sample from drying during analysis, several drops of the target solution were added between the glass slides. The swelling measurements were conducted at room temperature (25 °C), as well as at elevated temperatures of 60 °C and 80 °C. In case of the tests at elevated temperatures, the 24 h soaking period was carried out in an oven set to the target temperature. A steel plate comprising an adjustable heating cartridge was positioned on the microscope to maintain the target temperature during the measurement. Out-of-plane (z)-swelling was obtained by removing the samples from the solution and the thickness was rapidly recorded using a Mitutoyo micrometer gauge.

2.4.2. Volumetric Electrolyte Uptake

The volumetric electrolyte uptake was calculated from the measurement of dimensional change in any direction before and after soaking in KOH solution at a specific temperature using the following equation Equation (4):

$$\epsilon_m = \frac{V_{wet}(T, c_{KOH}) - V_{dry}(T)}{V_{wet}(T, c_{KOH})} \tag{4}$$

$V_{wet}(T, c_{KOH})$ is the wet volume of the membrane at a specific temperature and KOH concentration and $V_{dry}(T)$ is the dry polymer volume at a specific temperature T.

2.4.3. Ion Exchange Capacity

The ion exchange capacity (IEC) is defined as the number of accessible ions per gram of membrane polymer. It was measured using an $AgNO_3$ titration technique. A quantity of membrane polymer, ranging from 50–70 mg, was soaked for a period of 24 h in a solution of KCl at a temperature of 25 °C. Subsequently, the material was rinsed in deionized water. This process was repeated twice, after which the membrane samples were dried in an oven at 60 °C for 24 h. The dry weight of the exchanged membrane pieces is measured, and a 0.1 M $AgNO_3$ solution is prepared for conductometric titration with an automatic titrator of the type TITRANDO 888. Prior to titration with Cl^-, the dry polymer is transferred into 0.1 M $NaNO_3$ solution and allowed to soak for 24 h. The IEC of the polymer sample is calculated from the volume of $AgNO_3$ solution at the equivalence point according to Equation (5).

$$IEC = \frac{q_{ci} c_{AgNO_3} V_{AgNO_3}}{m_m^{dry}} \tag{5}$$

q_{ci} is the charge number of the exchanged counter ion, c_{AgNO_3} the concentration of the titration solution, V_{AgNO_3} the volume of titration solution and m_m^{dry} the measured dry weight of the membrane sample.

2.4.4. Gravimetrical Electrolyte Uptake

Membrane samples are cut into pieces measuring $5 \times 5\ cm$ in order to quantify gravimetric swelling. The samples are weighed in their delivery state and subsequently soaked for 24 h in accordance with the methodology outlined in Section 2.4.1 at the specified temperature. Subsequently, the samples are removed from the solution, briefly padded and weighed again. The authors are aware that rapid drying kinetics, particularly at elevated temperatures, may result in the falsification of the results and an underestimation of the gravimetric media uptakes. In the literature, the water uptake (WU_m) is commonly defined as follows Equation (6).[20]

$$WU_m = \frac{m_m^{wet}(T, c_{KOH}) - m_m^{dry}}{m_m^{dry}} \tag{6}$$

Given that polymers with larger IEC tend to exhibit increased swelling behavior, this work normalizes the water uptake to the IEC, thereby providing an expression for the hydration state, λ_m Equation (6).[21,22]

$$\lambda_m = \frac{WU_m(T, c_{KOH})}{M_{elec} IEC} \tag{7}$$

M_{elec} represents the molar mass of the electrolyte in used in the experiment. In this work KOH concentration between 0.1 and 1 M were used.

2.4.5. Hydrogen Permeability Through the Membrane

The permeability of hydrogen of the dry membrane was quantified *ex situ* within a permeation cell. The permeation cell comprises two distinct compartments, separated by the membrane sample. Both chambers are evacuated and flushed with hydrogen gas until the pressure reaches <1 $mbar$, after which the evacuation is repeated and the system is checked for any leakages. A hydrogen pressure of 2 bar in the first compartment and 1 bar in the second compartment was applied, resulting in a total differential pressure of 1 bar across the membrane. Subsequently, pressure sensors detect the rise in pressure within the second chamber over the course of 24–48 h (or until no differential pressure is present across the membrane). Given the known volume of the secondary chamber, membrane thickness δ_m, and membrane area A_{mem}, the permeability $P_{H_2}^{m,dry}$ can be calculated using the following equation Equation (8):

$$ln \frac{p_{H_2} - p_0}{p_{H_2} - p(t)} = \frac{P_{H_2}^{m,dry} A_{mem} RT}{\delta_m V_{chamber}} t \tag{8}$$

The pressure difference between the two chambers is denoted by $p_{H_2} - p_0$ and measurement value in the second chamber during the experiment is represented by $p(t)$. The gas constant R and the operating temperature T are used to calculate the permeation rate, which is expressed as a slope derived from the expression on the left side of equation Equation (8).

2.5. Theory and Modeling

Some assumptions must be made to model the concentration of gas and the resulting flux densities produced by the experimental procedure outlined in Section 2.3 First, gradients in the x/y direction are disregarded due to the limited cell area of 25 cm^2 and the high electrolyte flow rate. Consequently, mass transport of hydrogen predominantly occurs perpendicular to the membrane surface. Due to the high contacting pressures and the low in-plane contact resistances inside the cell, as well as the low manufacturing tolerances, the current densities are distributed homogeneously throughout the entire active area. Since the gas concentrations are obtained from stationary current steps, the total mass transport of hydrogen is expressed as a stationary mass balance, as shown in Equation (9).

$$\sum_i^n J_{H_2}^i = \sigma_{H_2} \tag{9}$$

The quantity $J_{H_2}^i$ represents the hydrogen flux density arising from a specific transport mechanism, designated by the subscript i. The sum of all the considered transport processes contributions (Figure 1) must be equal to the source of hydrogen, represented by σ_{H_2}, at the electrode. In this study, sink terms such as the recombination of hydrogen with oxygen to form water are neglected. Furthermore, other sink terms, such as ionic transport of hydroxide through the cell, commonly known as parasitic currents, are also excluded from consideration. The evolution of hydrogen at the catalyst particle is described by Faraday's law Equation (10), and thus represents the hydrogen source term σ_{H_2} in $mol/;m^2s$. The hydrogen evolves at the interface between the membrane and catalyst layer in the balance plane (Figure 1), resulting in the formation of a local hydrogen concentration, denoted as $c_{H_2}^*$. This assumption is crucial for modeling the experimental electrolysis in a zero-gap configuration. The presence of a gap at the interface between the electrode and the membrane introduces additional mass transport resistance, which significantly influences the hydrogen flux.[14]

$$\sigma_{H_2} = \frac{i_{H_2}}{2F} \tag{10}$$

In accordance with the mentioned assumptions, the evolving gas concentration at the catalyst particle gives rise to concentration gradients across the cell and membrane, which serve as a driving force for various mass transport processes, including electroosmotic drag, diffusion, and convection. These processes are illustrated in Figure 1. The mathematical description of these contributions is provided in the following subsections.

2.5.1. Mass Transport of Hydrogen into Bulk Solution

The mass transport at gas-evolving electrodes is a result of a complex interplay between pore diffusion, interfacial transfer from dissolved to gaseous hydrogen, bubble formation and the subsequent convection of the bubbles in the bulk electrolyte due to hydrodynamic forces.[16,23–25] The local gas concentration produced at the balance plane (Figure 1) can reach concentrations exceeding the saturation level of the surrounding bulk solution, resulting in local supersaturation and consequently, bubble formation. The maximum gas concentration, $c^*_{H_2}$, is therefore observed at the catalyst particle itself and decreases with increasing distance from the catalyst particle into the bulk solution. The minimum concentration is that of the saturated bulk solution $c^c_{H_2}$. The difference between these two concentration levels represents the driving force for diffusive transport of hydrogen from the catalyst layer into the bulk, either as gaseous or dissolved hydrogen. In order to describe the combined velocity of these processes, a mass transport coefficient k_l, in units of ms^{-1}, is introduced. The resulting flux density is defined as follows:

$$J^{Bulk}_{H_2} = k_l (c^*_{H_2} - c^c_{H_2}) \tag{11}$$

2.5.2. Hydrogen Diffusion in Anion Exchange Membranes

Given that the membrane is treated as a macroscopically homogeneous material, convective transport of hydrogen through the membrane is disregarded, leaving diffusion and drag as the dominating mechanisms through the membrane. The application of Fick's law of diffusion with the swollen membrane thickness δ_m as the diffusion length, yields the following expression for the diffusive contribution to the total hydrogen flux density given by Equation (12).

$$J^{Diff}_{H_2} = \frac{D^{eff}_{H_2}}{\delta_m} (c^*_{H_2} - c^a_{H_2}) \tag{12}$$

The effective diffusivity $D^{eff}_{H_2}$ is a function of different structure and morphological properties such as volumetric electrolyte uptake (ϵ_m) or the tortuosity (τ) of the transport channels inside the membrane. For PEM electrolyzers, correlations to estimate the effective diffusivity such as Bruggemann correlation is commonly applied using Equation (13).[15,26]

$$D^{eff}_{H_2} = \frac{\epsilon_m}{\tau} D^{elec}_{H_2} \tag{13}$$

A tortuosity of 1 indicates that the channels in the membrane are perfectly linear, with a length equal to the swollen thickness of the membrane. If the diffusivity is dominated by the transport through the membranes liquid channels the term $\epsilon_m D^{elec}_{H_2}$ represents the highest effective diffusivity possible. $D^{elec}_{H_2}$ is hereby the diffusivity in the pure liquid phase. In recent years, studies have been conducted to measure the tortuosity of membranes as the ratio of diffusion coefficients using nuclear magnetic resonance (NMR) techniques. It has been demonstrated that the volumetric electrolyte uptake exerts a pronounced influence on the tortuosity of the membrane, consequently affecting the diffusion pathway (Refs. [27,28]) In this work, the effective diffusivity $D^{eff}_{H_2}$ is determined and compared with theoretical diffusivities in the liquid and solid polymer.

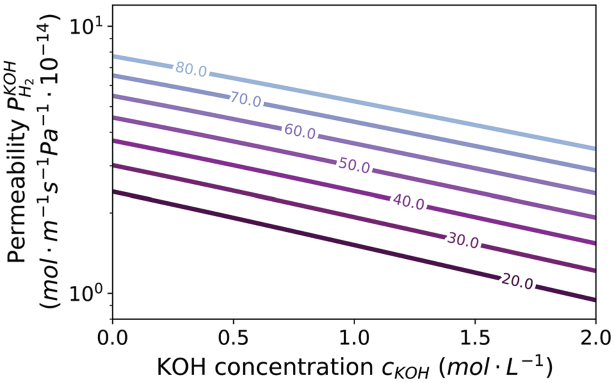

Figure 2. Calculated permeability of hydrogen in KOH solution between 0–2 *M* KOH and 20–80 °C from.[26,37,38]

2.5.3. Electroosmotic Drag of Hydrogen Through the Membrane

Hydrogen permeation can also occur due to the presence of dissolved hydrogen in the drag water of an electrolysis cell, as evidenced by ref. [13]. The electroosmotic drag is oriented in the same direction as the ionic flux through the membrane and is directly proportional to the current density applied to the system. This results in an increasing hydrogen flux with increasing hydroxide migration from cathode to anode. The expression for water drag is given in Equation (14).

$$J^{drag}_{H_2O} = \frac{i_{H_2}}{F} \xi \tag{14}$$

In this context, the variable ξ describes the drag coefficient and F the Faradaic constant. The drag coefficient represents the ratio of molecules that are dragged along with each ionic charge through the membrane. Literature on drag coefficients of anion exchange membranes is sparse. In a study conducted by Roy et al., the drag coefficient was observed to range from 2.5 to 8.15, dependent on the hydration state λ_m of the membrane, which ranged from 8 to 16 for a Tokuyama A201 membrane.[29] Given that the membrane employed in this study has a λ_m value of ≈4 (Figure 5), it was estimated that ξ would be within the range of 1–1.5. The monitoring of water levels during the experiment yielded a drag coefficient of 1, which was subsequently utilized in the model. As the AEM is operated with dissolved KOH as a liquid electrolyte, the

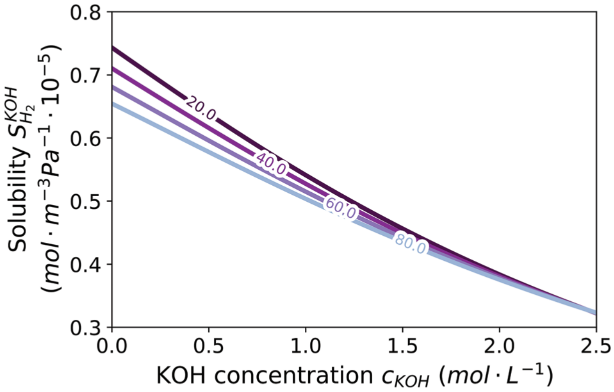

Figure 3. Calculated solubilities of hydrogen in KOH solution between 0 - 2 *M* KOH and 20–80 °C from,[26] note the inversed temperature dependency compared to the permeability.

concentration of the liquid electrolyte at the boundary layer, denoted by c^m_{elec}, is calculated via Equation (15).

$$c^m_{elec} = \frac{\rho(T, c_{elec})}{M_{elec}} \tag{15}$$

$\rho_{elec}(T, c_{elec})$ represents the density of the used electrolyte and M_{elec} the mean molar mass of the electrolyte solution. For a 1 M KOH solution at 60°C, the concentration results in 52 $\frac{mol}{l}$. The hydrogen flux from electroosmotic drag can finally be calculated by multiplying the drag water flux by the ratio of dissolved hydrogen per volume of electrolyte being transported through the membrane Equation (16).

$$J^{drag}_{H_2} = \frac{i_{H_2}}{F} \xi \frac{c^*_{H_2}}{c^m_{elec}} \tag{16}$$

2.5.4. Total Mass Transport and Supersaturation

The sum of all transport term leads to the final balance equation Equation (17). Note, that the diffusion terms through the membrane as well as from the balance plane into the bulk solution occur in opposing directions according to Figure 1.

$$\sigma_{H_2} = \frac{i_{H_2}}{2F} = J^{bulk}_{H_2} + J^{diff}_{H_2} + J^{drag}_{H_2}$$

$$= k_l(c^*_{H_2} - c^c_{H_2}) + \frac{D^{eff}_{H_2}}{\delta_m}(c^*_{H_2} - c^a_{H_2}) + \frac{i_{H_2}}{F} \xi \frac{c^*_{H_2}}{c^m_{elec}} \tag{17}$$

The concentration difference between the catalyst particle and the bulk electrolyte, denoted as $c^*_{H_2} - c^c_{H_2}$, is referred to as supersaturation.[30] Given that the hydrogen concentration in the bulk of the electrolyte is estimated as the saturation concentration at the operating pressure $p^c_{H_2}$, Henry's law can be applied ($c^c_{H_2} = p^c_{H_2} S^{elec}_{H_2}$). It is be assumed that the partial pressure of hydrogen in the anode compartment, $p^a_{H_2}$ is negligible, given that only minimal quantities of hydrogen (<< 4 %) are anticipated. Solving the resulting Equation (17) for $p^*_{H_2}$ leads to the final fitting function Equation (18).

$$p^*_{H_2} = \frac{\frac{i_{H_2}}{2F} + k_l S^{elec}_{H_2} p^c_{H_2}}{\frac{D^{eff}_{H_2}}{\delta_m} S^{elec}_{H_2} + k_l S^{elec}_{H_2} + \frac{i_{H_2}}{F} \frac{\xi S^{elec}_{H_2}}{c^m_{elec}}} \tag{18}$$

In order to apply the model to experimental data in the next section, it is necessary to calculate the flux density from the measured gas concentration at the anode, y_{H_2} according to Equation (19).

$$J^{exp}_{H_2} = \frac{y_{H_2}}{1 - y_{H_2}} \frac{i}{4F} = J^{diff}_{H_2} + J^{drag}_{H_2} \tag{19}$$

Fitting experimental hydrogen flux data at different current densities to Equation (18) the parameters k_l and $D^{eff}_{H_2}$ are obtained.

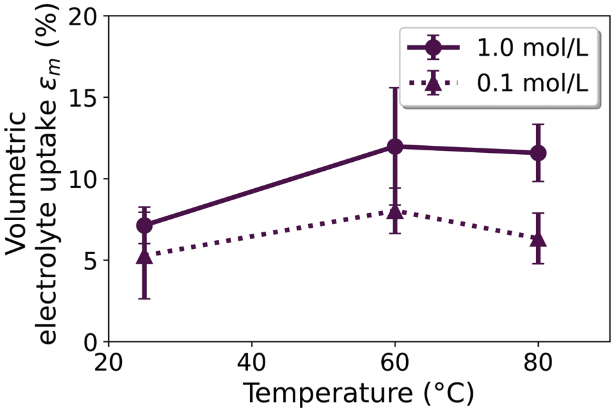

Figure 4. Measured volumetric electrolyte uptake at 25 °C, 60 °C, and 80 °C at 0.1 *M KOH* and 1 *M KOH*.

3. Results and Discussion

3.1. Physio-Chemical Membrane Characteristics

In the context of water electrolysis, particularly within the experimental configuration described in Section 2.3, the membrane is fully immersed in electrolyte with a concentration of 1 *MKOH*. The wetting of the membranes results in the uptake of electrolyte due to the hydrophilic domains that are formed as a consequence of the ionic functional groups present in the membrane polymer. It has been demonstrated that hexamethyl-p-terphenylbenzimidazolium (HMT-PMBI) membranes exhibit the formation of percolating networks of hydrophilic pores at higher hydration levels (λ = 3 - 9), which serve as transport channels for ionic conduction.[31] In their study, Sayema K. Tuli et. al. demonstrated that the conductivity of a polystyrene-based AEM submerged in a 0 – 10 *M KOH* solution exhibited an increase to ≈3 *M* KOH, followed by a decline at higher concentration levels. This suggests that the morphology and the channels forming inside the AEM significantly influence the ion transport mechanism.[32] For example, the presence of excess water within the AEM at higher hydration levels (λ_m) has been observed to reduce the charge density, consequently leading to a decrease in

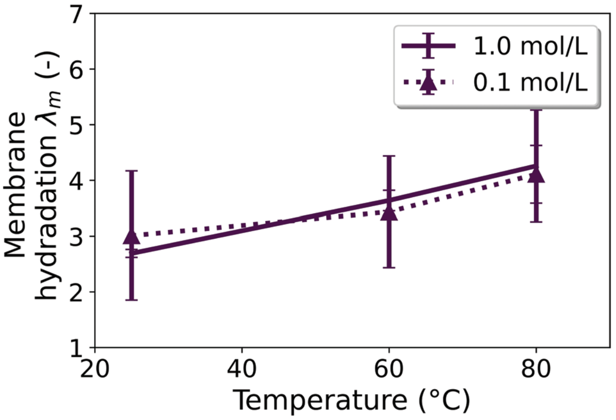

Figure 5. Measured hydration states at 25 °C, 60 °C, and 80 °C at 0.1 *M KOH* and 1 *M KOH*.

conductivity.[32–34] It is conceivable that the percolating network formed from the electrolyte inside the AEM may act as a pathway for hydrogen permeation as well, depending on the size and shape of the network. Kang et al. employed an electrochemical method at low current densities, disregarding all mass transport resistances within the cell, to measure the hydrogen permeation rate. Their findings revealed a notable enhancement in the hydrogen permeation rate of the hydrated membrane.[35] A mixed percolation model was proposed, whereby the electrolyte channel forms both clusters and channels, thus enabling the permeation of hydrogen through a number of solution and diffusion steps. However, in their experimental setup, the membrane is not submerged in a KOH solution, as in case of electrolysis operation. To date, there have been no reported measurements of hydrogen permeation in fully submerged KOH conditions. In order to model the membrane's ability to transport hydrogen, the hydrogen permeation through the dry polymer and the liquid phase is compared.

The permeability $P_{H_2}^m$ of hydrogen through a specific material m at a given temperature T is given by the product of the diffusivity $D_{H_2}^m$ and solubility $S_{H_2}^m$ according to Equation (20). The solubility represents the equilibrium concentration of hydrogen in the material, whereas the diffusivity denotes the velocity of hydrogen portion traveling through a specific material (liquid or solid).

$$P_{H_2}^m = D_{H_2}^m S_{H_2}^m \tag{20}$$

Kim et al. demonstrated for perfluorosulfonic acid membranes that the permeability exhibited a nearly twofold increase when the membrane was fully hydrated and submerged in water.[36] The liquid phase within the AEM-polymer might therefore play a pivotal role in the transport of hydrogen. In order to facilitate a comparative analysis of the permeabilities exhibited by the polymer and the liquid electrolyte within the AEM, data from literature and the measured permeabilities of the membrane are compared in the following.

The solubilities of hydrogen in liquid electrolyte in the range from 10 °*C* to 90 °*C* and 0 to 30 %*wt*. KOH are used from Schalenbach et al.[26] The diffusivities were derived from the data presented by Thams et al.[37] The equations derived from literature data to calculate solubilities and diffusivities are presented in the Supporting Information. Mass quantities are converted to molar quantities by applying a correlation for the density of the electrolyte in the desired temperature and concentration range from Gilliam et al.[38] The calculated permeability in liquid electrolyte from Equation (20) and the solubilities of hydrogen at varying KOH concentrations and temperatures are illustrated in **Figures 2** and **3**, respectively.

As illustrated in Figure 3, the solubilities of hydrogen in KOH solution exhibit an expected decline with increasing temperature within the specified range. The solubilities reach a value of 5.4 $\times\ 10^{-6} molm^{-3}\ Pa$ at 25 °*C* and 4.9 $\times\ 10^{-6} molm^{-3}\ Pa$ at 60 °*C* in 1*MKOH*. In contrast, the permeability-temperature dependency is reversed. The diffusivity of hydrogen dominates the total permeation rate in the liquid phase since the permeability increases with increasing temperature. A value of $7.4 \times 10^{-9} m^2 s^{-1}$ at 60 °*C* is used to compare the later derived effective diffusivity through the membrane from experimental data.

The permeability of hydrogen through the polymeric phase of the membrane was measured at 25 °*C* in accordance with the procedure outlined in Section 2.4.5, yielding 0.23 $\times\ 10^{-14}\ mol(m\, s\, Pa)^{-1}$. The permeability of hydrogen in the dry polymer is with $1.71 \times 10^{-14}\ mol(m\, s\, Pa)^{-1}$ roughly one order of magnitude lower than the value through the liquid phase at the same

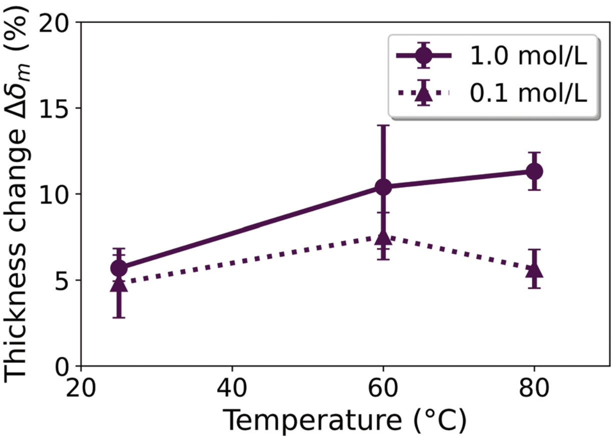

Figure 6. Measured dimensional change of the membrane thickness at 25 °C, 60 °C, and 80 °C at 0.1 *M KOH* and 1 *M KOH*.

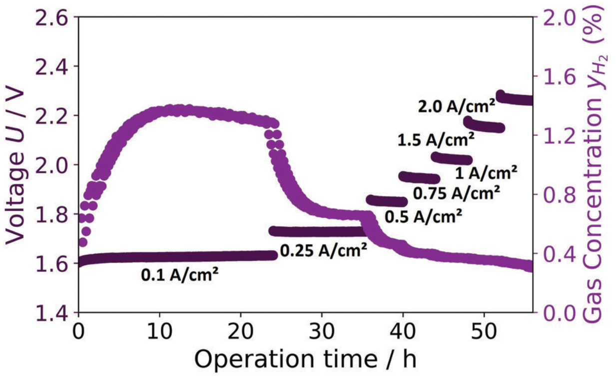

Figure 7. Measured cell voltage and gas concentration of hydrogen in oxygen at 60 °C in 1 *M* KOH from 0.1 to 2 Acm^{-2} on a 25 cm^2 single cell.

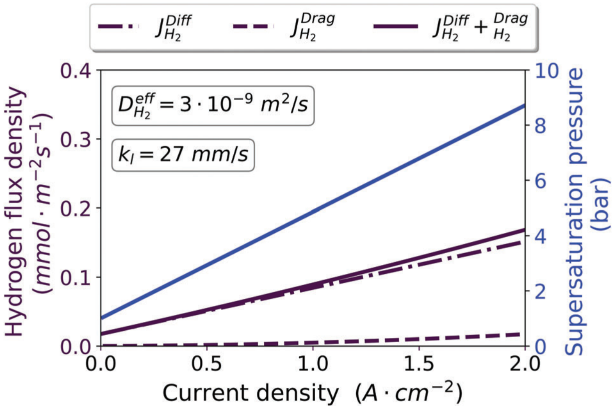

Figure 8. Measured permeation flux densities and calculated suration pressure $p_{H_2}^{*}$ from the mass transport model at 60 °C in 1 M KOH from 0.1 to 2 Acm^{-2} on a 25 cm^2 single cell.

temperature (Figure 2). This indicates that depending on the electrolyte uptake ϵ_m in the membrane, the contribution of the solid phase of membrane potentially needs to be considered for the hydrogen transport.

Approximately 10.5 % of the membrane's volume is occupied by the electrolyte in 1 $M\ KOH$ at 60 °C as shown in **Figure 4**. The membrane is already completely saturated at 60 °C and the ionic groups within the membrane are fully hydrated. A further temperature increase does not result in a significant increase in the electrolyte content of the membrane. The hydration level in **Figure 5**, which remains largely unchanged throughout the entire measurement range supports this observation. An increase of 1 in λ_m is observed in a temperature range from 25 °C to 80 °C. At 60 °C, ≈3.5 molecules of water associate with each ionic group of the membrane. Given that the number of water molecules per ionic group, λ_m, remains constant while the volumetric electrolyte uptake, ϵ_m, increases, it can be inferred that the swelling occurs as a result of the electrolytes filling the channels within the membranes.

The swollen thickness of the membrane δ_m is the minimum permeation distance and therefore influences the permeation characteristics according to Equation (12). The total thickness is calculated from the equation given in Equation (21) using the measured thickness change depicted in **Figure 6**, which correspond to the dry membrane thickness $\delta_{m,\,dry}$ of 76 μm.

$$\delta_m = (\triangle\delta_m + 1)\delta_{m,dry} \tag{21}$$

At a temperature of 60 °C and a solution of 1 $M\ KOH$, the total thickness is found to be 85 μm, resulting in a considerably larger transport pathway than observed at 25 °C. The thickness increase $\triangle\delta_m$ with increasing temperature, exhibits a similar trend to the volumetric electrolyte uptake.

Table 2. Parameters used in the model to simulate gas crossover at operating conditions (60 °C, 1 $M\ KOH$).

Operating state					Membrane properties			
T / °C	p_c / bar	V_{elec} / $\frac{ml}{min}$	ϵ_m /%	λ_m / -	δ_m / μm	ξ_m/-	IEC / $\frac{meq}{mol}$	ρ_{dry} / $\frac{kg}{m^3}$
60	1	200	10.5	3.5	84	1	1.5	961.6

Using the diffusivities $D_{H_2}^{elec}$ and solubilities $S_{H_2}^{elec}$ in the liquid electrolyte and the swelling data from Figures 4–6 the derived model is fully parameterized and applied to experimental data in the next sections.

4. Model Verification

The electrolysis cell used to measure the gas concentration showed a performance of 2.01V at 1.0Acm^{-2} with a $Ni(OH)_2$ anode catalyst. At the final current stage, following a total operational period of 56 h, the cell attained a voltage of 2.2 V at 2.0 Acm−2. The upper limit of 2 % hydrogen in oxygen is not reached at any current density, thereby ensuring the safe operation of the system even at low current densities up to 5% partial load (0.1 Acm^{-1}). The lowest measured hydrogen concentration with 0.37 % was reached at 2.0 Acm^{-2} (**Figure 7**). During the initial 10 h of the electrolysis, the hydrogen content in the anode gas increased to 1.36 % at 0.1 Acm^{-2}. A slight decline is evident, reaching ≈ 1.28 % after 24 h. Nevertheless, the observed decrease in hydrogen concentration during the initial period of the electrolysis process (10–24 h) suggests a rearrangement or dislocation of catalyst particles (**Figure 11**) on the surface of the electrode, resulting in the formation of transport channels for hydrogen. This could lead to a decrease in the mass transport resistance into the bulk solution of the overall electrode and thus to a decrease in the gas concentration at the anode. A significant change in the catalyst would result in a change in the overpotential, which is not observed in the cell voltage.

A slight voltage drift of 30 mV was observed between 0 and 6 h during operation, indicating that the system was stabilizing. The voltage remains constant for a period of 18 h until the next current step is applied. Following the initial current step from 0.1 to 0.25 Acm^{-2}, the system becomes stable, and fluctuations in the measured hydrogen gas concentrations become negligible.

The hydrogen flux densities of the measured hydrogen concentrations were calculated using Equation (19), resulting in values ranging from 0.02 $mmol(m^2s)^{-1}$ at 0.1 Acm^{-2} to 0.16 $mmol(m^2s)^{-1}$ at 2 Acm^{-2}. The flux increases linearly with a slope of 0.08 $mmolAs^{-1}$ with increasing current density. At low current densities, the hydrogen flux is relatively high in comparison to the oxygen being produced, resulting in a higher gas concentration. Further increase of the current density leads to a decreasing hydrogen concentration at the anode and is attributed to the dilution of the hydrogen flux by the evolving oxygen at the anode. A similar order of magnitude for the hydrogen flux have been reported in studies by Trinke et al. for PEM and Rodrigo Lira Garcia Barros et al. for alkaline systems.[14,16] The observed increasing flux density indicates a increasing supersaturation at the cathode with increasing current density, arising from mass transport resistances inside the cell. The maximum permeation flux density resulting electroosmotic drag reaches 0.015 · $mmol(m^2s)^{-1}$ at 2 Acm^{-2} and is illustrated in **Figure 8**. Given that the estimated drag coefficient is 1 and the drag contribution increases with the current density, at 2 Acm^{-2}, ≈ 10 % of the total hydrogen flux can be attributed to electroosmotic drag. Since, the safety-relevant hydrogen concentrations occur at low current

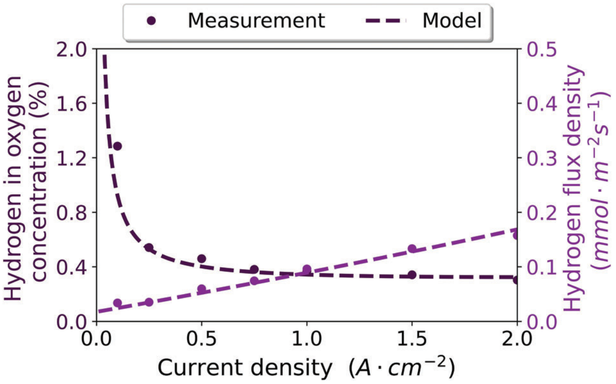

Figure 9. Measured and resulting gas concentration at the anode at 60 °C in 1 M KOH from 0.1 to 2 Acm^{-2} on a 25 cm^2 single cell.

densities, it can be concluded that electroosmotic drag has a negligible influence on the hydrogen crossover for this particular membrane but must be considered for membranes with higher drag coefficients ξ.

In order to quantify the mass transport coefficient of the electrode as well as the effective hydrogen diffusivity through the membrane, the developed mass transport model is applied. The parameters employed are summarized in **Table 2** and Equation (18) is fitted to the measured flux densities. The mass transport coefficient k_l and an effective diffusivity of $D^{eff}_{H_2}$ are determined to 27 mms^{-1} and $3.0 \times 10^{-9} m^2s^{-1}$. The magnitude of the effective diffusivity is in the range of the by Trinke et al. reported values for PEM membranes.[39] The predicted hydrogen concentration from Equation (19) correlates closely with the measured hydrogen concentrations (**Figure 9**). This supports the assumption of a constant k_l for this particular electrode and setup. A constant k_l with increasing current density indicates, that even at low current densities between $0 and 0.5 Acm^{-2}$ the electrode enables an efficient bubble removal, without significant further improvement due to drag and coalescence of surrounding bubbles with increasing current density. The removal of hydrogen through the electrode in lateral direction is therefore rather quick and lies in the range of reported k_l values for PEM cathodes.[15]

The determined effective diffusivity $D^{eff}_{H_2}$ of $3.0 \times 10^{-9} m^2s^{-1}$ is ≈2.5 times lower than the diffusivity in the bulk electrolyte but 3 times higher than the theoretical diffusion through the liquid domain of the membrane only ($\epsilon_m D^{elec}_{H_2} = 7.8 \times 10^{-10} m^2s^{-1}$). Using Equation (13) the theoretical tortuosity of the membrane would be ≪1, indicating the hydrogen would not only take pathways through the liquid portion of the membrane. An explanation could be, that during the swelling process the polymer chains align, forming more linear channels, which reduce the tortuosity of the membrane polymer and increase the effective diffusivity through the polymer phase. Furthermore, the hydrogen undergoes potentially several solution and diffusion processes in the polymer matrix further increasing the effective diffusivity and decreasing the theoretical tortuosity. This emphasizes the importance of the membranes microstructure to be tunable to higher transport resistances.

The Sherwood number, as defined in Equation (22), compares the transport velocity through the electrode with diffusion through the membrane. The total mass transport through the catalyst layer is ≈770 times faster than the transport through the membrane. For such reason the transport resistances arising from the membrane properties are significantly higher than those from the catalyst layer (**Figure 10**). A further reduction in the hydrogen gas concentration at the anode necessitates a decrease in the transport resistance of the cathode, while the membrane transport resistance must increase.

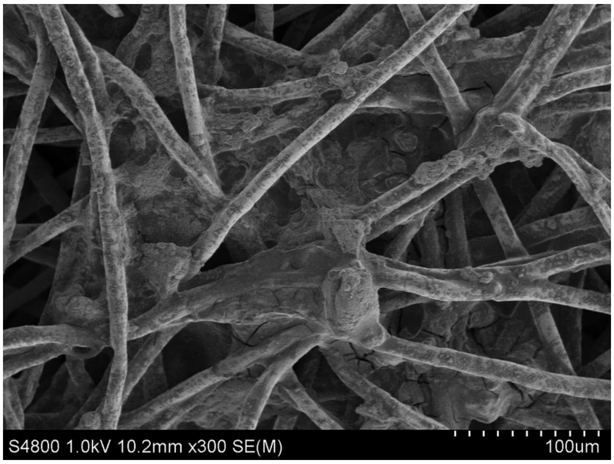

Figure 10. Catalyst layer structure on a Siemens Energy PTL, particle catalyst and ionomer forms island bond to fibers of the substrate.

$$Sh = \frac{k_l \delta_m}{D^{eff}_{H_2}} \tag{22}$$

The resulting theoretical pressure at the catalyst calculated by Equation (18) using the derived parameters k_l and $D^{eff}_{H_2}$, reaches values of up to 8.8 bar at 2 Acm^{-2}. The resulting 8.8-fold supersaturation is in the order of magnitude of reported supersaturation values.[13,40] A reduction of the supersaturation, by increasing the transport properties of the electrode namely k_l reduces

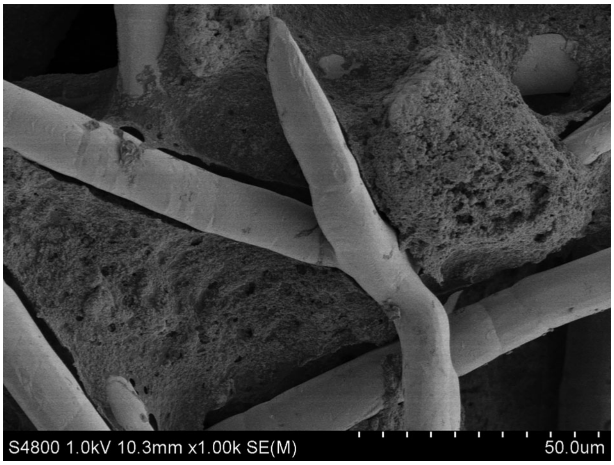

Figure 11. Catalyst layer structure on a Siemens Energy PTL, catalyst island show macropores in the micrometer range.

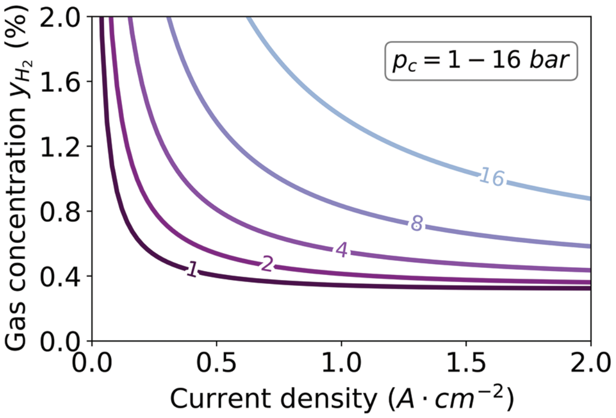

Figure 12. Simulated influence of the operating pressure between 1 and 16 *bar* on the gas concentrations with constant k_l, $D_{H_2}^{eff}$ and parameters from Table 2, exp. value: 1 bar.

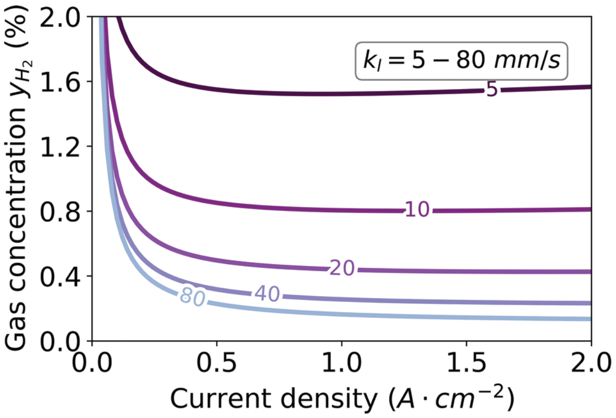

Figure 13. Simulated influence of mass transport coefficient of the electrode between 5 and 80 mms^{-1} at 1*bar*, a constant $D_{H_2}^{eff}$ and parameters from Table 2, exp. value: 27 mms^{-1}.

the amount of dissolved hydrogen carried by diffusion and drag through the membrane.

The diffusive hydrogen flux is observed to increase with current density, due to the increased concentration difference from the cathode to the anode, reaching a maximum value of 0.14 $mmol(m^2s)^{-1}$ at 2 Acm^{-2}. The extrapolated hydrogen flux density at 0 Acm^{-2} reaches 0.02 $mmol(m^2s)^{-1}$ and represents the only the diffusive contribution driven by the hydrogen partial pressure difference between anode and cathode. The hydrogen flux density at 0 Acm^{-2} is predominantly influenced by the structure of the membrane and the dominant diffusion pathway of the hydrogen through the membrane. Nonetheless, in case of higher operating pressures of the electrolyzer, the initial diffusion flux will likely increase and may constrain the safely achievable minimum partial load of the electrolyzer.

4.1. Influence of Pressure, Mass Transport and Membrane Properties

In **Figure 12** the resulting hydrogen concentrations at the anode simulated in the pressure range from 1 to 16 *bar*. For ambient conditions and a pressure of 2 *bar* the gas concentration stays under 2 % which corresponds to a partial load operation of under 20 %. At 16 *bar* however, the minimal operating current densities reaches up to 0.8 Acm^{-2}, resulting in decreased dynamic capabilities of the electrolyzer.

Enhancing the mass transport in the electrode and therefore reducing the supersaturation at higher current densities, does slightly increase the partial load capability as shown in **Figure 13**. An increase of k_l from 5 − 80 mms^{-1} reduces the gas concentration by almost 90% at the nominal operating (2 Acm^{-2}) and shifts the minimum partial load current density from 0.2 to 0.1Acm^{-2}. Further increase of the electrolyzer's partial load capability, especially at higher operating pressures, should come from membrane improvements. Increasing the thickness of the membrane and therefore the diffusion pathway through the membrane while maintaining the volumetric electrolyte uptake, influences the gas crossover proportionally according to Equation (19). A thicker membrane increases the ohmic resistance and is disadvantageous for the overall efficiency of the electrolyzer. An improvement of the microstructure of membrane especially parameters influencing the effective diffusion coefficient will be favorable.

The highest theoretical diffusivity of the hydrogen is reached in the liquid phase of the membrane with a tortuosity of 1. The contribution of the liquid diffusion is estimated by $\epsilon_m D_{H_2}^{elec}$. The diffusive contribution in the solid polymer phase, which is presented by $(1 - \epsilon_m) D_{H_2}^{poly}$ is calculated by Equation (24).

$$D_{H_2}^{eff} = \epsilon_m D_{H_2}^{elec} + (1 - \epsilon_m) D_{H_2}^{poly} \tag{23}$$

$$D_{H_2}^{poly} = \frac{D_{H_2}^{eff} - \epsilon_m D_{H_2}^{elec}}{1 - \epsilon_m} \tag{24}$$

The estimated diffusivity $D_{H_2}^{poly}$ results in $2.4 \times 10^{-9}\ m^2 s^{-1}$ and is almost 4 times lower than the diffusivity through the electrolyte. In contrast the permeabilities of the polymer at 25 °*C* had been determined to be ≈8 times lower than the permeability in the

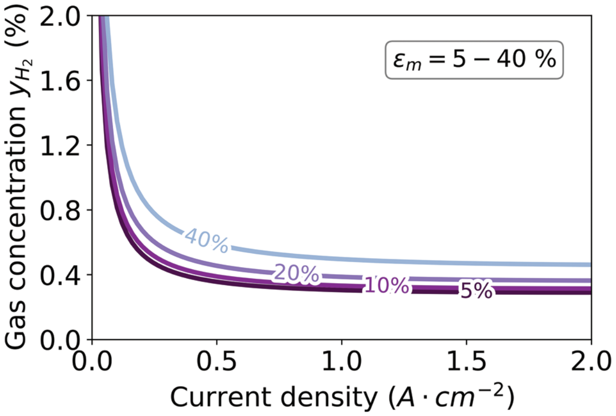

Figure 14. Simulated influence of the volumetric electric uptake of the membrane between 5 and 40 %, with parameters from Table 2, exp. value: 10.5 %.

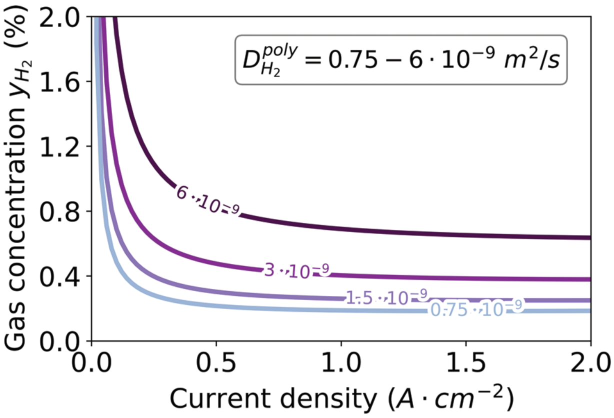

Figure 15. Simulated influence of polymer diffusivity of the membrane between 0.75 and 6 × $10^{-9}\ m^2s^{-1}$ with parameters from Table 2, exp. value: 2.4 × $10^{-9}\ m^2s^{-1}$.

electrolyte. An explanation for the higher diffusivity in the polymer phase could be the dominance of the temperature dependence of diffusion coefficient. The volumetric electrolyte uptake is already low and leads to a potentially low phase segregation resulting in small contribution of the liquid domain to the total diffusivity. Further improvement of the volumetric electrolyte uptake does not significantly increase the partial load capability according to **Figure 14**. However decreasing the solid polymer diffusivity for instance by changing the microstructure of the polymer, does significantly improve the crossover characteristics (**Figure 15**). Lowering the diffusivity by a factor of 3 to ≈0.75 × $10^{-9}\ m^2s^{-1}$ would result in a minimum partial load of $0.02 Acm^{-2}$ at 1 *bar* (Figure 15) and 0.4 Acm^{-1} at 16 *bar*. A potential higher tortuosity for both liquid and solid phases of the membrane would be beneficial to further reduce the crossover and increase the partial load capability.

ϵ_m and $D^{poly}_{H_2}$ are the result of the morphological microstructure and have been used in this study do describe the transport properties of the membrane. The model predicts that modifying the membrane morphology has a more pronounced impact on the gas crossover than increasing the thickness of the membrane. Notably, at low current densities, the dynamic capabilities are markedly enhanced by creating a membrane with high tortuosity, low polymer diffusivity and minimal electrolyte content. By reducing the electrolyte content to a minimum value, that does not compromise the membrane conductivity, a membrane with a high resistance to hydrogen mass transport, while maintaining the electrolyzer efficiency, seems most well-suited for AEM electrolyzer stacks.

5. Conclusion

This work shows that the gas cross over in AEMs with low drag coefficients can well be described by a mass balance of hydrogen travelling through the membrane and the electrode. An effective hydrogen diffusivity through the membrane and a mass transport coefficient through the electrode was obtained. The effective hydrogen diffusivity in the soaked membrane has been determined to 3 × $10^{-9} m^2 s^{-1}$, which is surprisingly high compared to the diffusivity in pure liquid electrolyte (7.4 × $10^{-9} m^2 s^{-1}$, 1 M KOH, 60 °C). The membranes microstructure was found to be key for low current density operation to control gas transport in the electrolyzer. A hydrogen in oxygen concentration of 1.28 % at low partial load conditions of 0.1 Acm^{2-1} and 0.37 % at maximum load conditions of 2 Acm^{-2} were obtained. Safe operation conditions of the electrolyzer can be found within a large dynamic range suitable for renewable energy profiles at ambient conditions. In conclusion, the low crossover of the AF3-HWK9-75-X membrane can be attributed to its low volumetric water uptake and low diffusivity in the polymer. A further decrease may be achievable by increasing the membrane's tortuosity. Therefore, modifying the microstructure of the membrane offers significant potential for future membranes with even larger transport resistances for hydrogen, while maintaining high electrolyzer efficiency.

Supporting Information

Supporting Information is available from the Wiley Online Library or from the author.

Acknowledgements

The investigations were partly funded by the BMBF under the contract number AEMready (FKZ:03SF0613B).

Conflict of Interest

The authors declare no conflict of interest.

Data Availability Statement

The data that support the findings of this study are available from the corresponding author upon reasonable request.

Keywords

AEM, gas crossover, membrane properties, mass transport coefficient

Received: July 29, 2024
Revised: November 3, 2024
Published online: December 19, 2024

---

[1] N. Rambhujun, M. S. Salman, T. Wang, C. Pratthana, P. Sapkota, M. Costalin, Q. Lai, K.-F. Aguey-Zinsou, *MRS Energy Sustain.* **2020**, *7*, 1.
[2] *Electrochemical Power Sources: Fundamentals, Systems, and Applications: Hydrogen Production by Water Electrolysis*, (Eds.: T. Smolinka, J. Garche), Elsevier, San Diego **2022**.
[3] International Energy Agency, Global hydrogen review 2023, **2023**.
[4] Irena, *Green Hydrogen Cost Reduction: Scaling up Electrolysers to Meet the 1.5°C Climate Goal*, Irena, Abu Dhabi **2020**.
[5] P. Chen, X. Hu, *Adv. Energy Mater.* **2020**, *10*, 39.
[6] L. Fischer, S. S. Hartmann, A. Maljusch, C. Däschlein, O. Prymak, M. Ulbricht, *J. Membr. Sci.* **2023**, *669*, 121306.
[7] A. Maljusch, Presentation, Program Workshop Advanced Alkaline Electrolysis, Fraunhofer Institute for Manufacturing Technology and Materials (IFAM), Dresden, Germany **2020**.

[8] Z. Liu, S. D. Sajjad, Y. Gao, H. Yang, J. J. Kaczur, R. I. Masel, *Int. J. Hydrogen Energy* **2017**, *42*, 29661.

[9] T. Huang, X. Qiu, J. Zhang, X. Li, Y. Pei, H. Jiang, R. Yue, Y. Yin, Z. Jiang, X. Zhang, M. D. Guiver, *J. Power Sources* **2022**, *527*, 231143.

[10] M. Moreno-González, P. Mardle, S. Zhu, B. Gholamkhass, S. Jones, N. Chen, B. Britton, S. Holdcroft, *J. Power Sources Adv.* **2023**, *19*, 100109.

[11] W. Chen, M. Mandal, G. Huang, X. Wu, G. He, P. A. Kohl, *ACS Appl. Energy Mater.* **2019**, *2*, 2458.

[12] S. A. Grigoriev, V. I. Porembskiy, S. V. Korobtsev, V. N. Fateev, F. Auprêtre, P. Millet, *Int. J. Hydrogen Energy* **2011**, *36*, 2721.

[13] M. Schalenbach, M. Carmo, D. L. Fritz, J. Mergel, D. Stolten, *Int. J. Hydrogen Energy* **2013**, *38*, 14921.

[14] R. Lira Garcia Barros, J. T. Kraakman, C. Sebregts, J. van der Schaaf, M. T. de Groot, *Int. J. Hydrogen Energy* **2024**, *49*, 886.

[15] P. Trinke, B. Bensmann, R. Hanke-Rauschenbach, *Int. J. Hydrogen Energy* **2017**, *42*, 14355.

[16] P. Trinke, P. Haug, J. Brauns, B. Bensmann, R. Hanke-Rauschenbach, T. Turek, *J. Electrochem. Soc.* **2018**, *165*, F502.

[17] S. Oikonomidis, M. Ramdin, O. A. Moultos, A. Bos, T. J. Vlugt, A. Rahbari, *Int. J. Hydrogen Energy* **2023**, *48*, 34210.

[18] K. T. Malkow, A. Pilenga, D. Blagoeva, Eu harmonised terminology for hydrogen generated by electrolysis: An open and comprehensive compendium, https://op.europa.eu/en/publication-detail/-/publication/ef4e10c2-ee7f-11eb-a71c-01aa75ed71a1/language-en/format-PDF/source-280217337 (accessed: November 2023).

[19] Ionomr Innovations Inc, Aemion+ ®reinforced membranes for water electrolysis: Apn-aem-1007-b, **2023**, https://www.ionomr.com (accessed: November 2023).

[20] K. M. Meek, C. M. Antunes, D. Strasser, Z. R. Owczarczyk, A. Neyerlin, B. S. Pivovar, *ECS Trans.* **2019**, *92*, 723.

[21] G. Huang, M. Mandal, N. U. Hassan, K. Groenhout, A. Dobbs, W. E. Mustain, P. A. Kohl, *J. Electrochem. Soc.* **2021**, *168*, 024503.

[22] M. A. Vandiver, B. R. Caire, J. R. Carver, K. Waldrop, M. R. Hibbs, J. R. Varcoe, A. M. Herring, M. W. Liberatore, *J. Electrochem. Soc.* **2014**, *161*, H677.

[23] L. J. J. Janssen, *J. Appl. Electrochem.* **1987**, *17*, 1177.

[24] L. Janssen, J. G. Hoogland, *Electrochim. Acta* **1973**, *18*, 543.

[25] H. Vogt, *J. Appl. Electrochem.* **1989**, *19*, 713.

[26] M. Schalenbach, W. Lueke, D. Stolten, *J. Electrochem. Soc.* **2016**, *163*, F1480.

[27] P. Knauth, L. Pasquini, R. Narducci, E. Sgreccia, R.-A. Becerra-Arciniegas, M. L. Di Vona, *J. Membr. Sci.* **2021**, *617*, 118622.

[28] Q. Zhao, P. Majsztrik, J. Benziger, *J. Phys. Chem. B* **2011**, *115*, 2717.

[29] A. L. Roy, J. Peng, T. A. Zawodzinski, *ECS Meet. Abstr.* **2018**, *MA2018-01*, 1755.

[30] S. Shibata, *Bull. Chem. Soc. Jpn.* **1963**, *36*, 53.

[31] E. M. Schibli, A. G. Wright, S. Holdcroft, B. J. Frisken, *J. Phys. Chem. B* **2018**, *122*, 1730.

[32] S. K. Tuli, A. L. Roy, R. A. Elgammal, M. Tian, T. A. Zawodzinski, T. Fujiwara, *J. Membr. Sci.* **2018**, *565*, 213.

[33] T. J. Peckham, S. Holdcroft, *Adv. Mater. (Deerfield Beach, Fla.)* **2010**, *22*, 4667.

[34] P. M. Mangiagli, C. S. Ewing, K. Xu, Q. Wang, M. A. Hickner, *Fuel Cells* **2009**, *9*, 432.

[35] Z. Kang, M. Pak, G. Bender, *Int. J. Hydrogen Energy* **2021**, *46*, 15161.

[36] S. Kim, J. Song, B. T. Duy Nguyen, J. Lee, J. Seong, S. Nam, S. So, J. F. Kim, *Chem. Eng. J.* **2023**, *471*, 144696.

[37] M. J. Tham, R. D. Walker, K. E. Gubbins, *J. Phys. Chem.* **1970**, *74*, 1747.

[38] R. GILLIAM, J. GRAYDON, D. KIRK, S. THORPE, *Int. J. Hydrogen Energy* **2007**, *32*, 359.

[39] P. Trinke, G. P. Keeley, M. Carmo, B. Bensmann, R. Hanke-Rauschenbach, *J. Electrochem. Soc.* **2019**, *166*, F465.

[40] T. Sakai, H. Takenaka, N. Wakabayashi, Y. Kawami, E. Torikai, *J. Electrochem. Soc.* **1985**, *132*, 1328.